Synthesis, Structure, and Properties of the Complex Zintl Phase Eu9Zn4.5As9: A Candidate Topological Insulator and Thermoelectric Material

Spencer R. Watts [1], Olha Pokhvata [1], Bhushan Thipe, Xiaojian Bai, Svilen Bobev [*], Sviatoslav Baranets [*]

Posted Date: 27 January 2026

doi: 10.20944/preprints202601.1941.v1

Keywords:

Zintl phases; thermoelectric materials; magnetic materials; single-crystal X-ray diffraction; crystal structures; structural disorder

Article

Synthesis, Structure, and Properties of the Complex Zintl Phase $Eu_9Zn_{4.5}As_9$: A Candidate Topological Insulator and Thermoelectric Material

Spencer R. Watts[1,‡], Olha Pokhvata[1,‡], Bhushan Thipe[2], Xiaojian Bai[2], Svilen Bobev[3,*] and Sviatoslav Baranets[1,*]

[1] Department of Chemistry, Louisiana State University, Baton Rouge, Louisiana 70803, USA
[2] Department of Physics and Astronomy, Louisiana State University, Baton Rouge, Louisiana 70803, USA
[3] Department of Chemistry and Biochemistry, University of Delaware, Newark, Delaware 19716, USA
* Correspondence: sbaranets@lsu.edu, bobev@udel.edu
‡ These authors contributed equally.

Abstract

Reported are the synthesis and the detailed analysis of the crystal and electronic structure of the novel Zintl phase $Eu_9Zn_{4.5}As_9$. This material was identified in the densely populated Eu–Zn–As compositional space. For structure determination and for property measurements, suitable single crystals of this compound were grown from either Sn- or Pb-flux. Single-crystal X-ray diffraction methods indicate that $Eu_9Zn_{4.5}As_9$ crystallizes in the orthorhombic crystal system with the space group *Pnma* (a = 12.1953(7) Å, b = 4.3730(2) Å, c = 42.674(2) Å) and is formally isostructural to $Ca_9Mn_{4+x}Sb_9$, the less common "9–4–9" type. The structure is heavily disordered, with multiple partially occupied sites, yet, according to the Zintl-Klemm formalism, a charge-balanced composition $(Eu^{2+})_9(Zn^{2+})_{4.5}(As^{3-})_9$ is attained. Electronic structure calculations for a model, disorder-free structure indicate no energy gap between the valence and the conduction bands, and suggest a (semi)metallic behavior. Preliminary susceptibility measurements confirm the expected divalent nature of Eu^{2+} ([Xe] $4f^7$ ground state).

Keywords: Zintl phases; thermoelectric materials; magnetic materials; single-crystal X-ray diffraction; crystal structures; structural disorder

1. Introduction

Zintl phases are intermetallic compounds, characterized by the simultaneous coexistence of covalent and ionic bonding interactions in their structures. Formed from groups 1, 2, or lanthanide metals and the more electronegative early post-transition elements from groups 13–15, the crystal structures of these materials often exhibit unique (poly)anionic frameworks. The charge-balance requirements according to the Zintl-Klemm concept [1] are satisfied if one considers ionic-like interactions between the elements with differing electronegativities. The structural complexity that arises from this formalism is thought of as both the hallmark of Zintl phases and an important element in the design of materials with unique physical properties [2].

Zintl pnictides, the largest group of Zintl phases that have been discovered thus far, arise from combinations of the aforementioned less electronegative metals with the pnictogen elements P, As, Sb, and Bi (*Pn* hereafter). The unique chemistry of these materials allows them to form a large variety of homoatomic *Pn*–*Pn* and heteroatomic *Pn*–*M* bonds (*M* = transition metals and Group 13/14 elements), which result in unique and complex structural motifs [3]. These combinations often yield narrow bandgaps and enhanced transport properties [4–6]. As a result, much progress surrounding the study of Zintl pnictides has been dedicated to the study of their potential toward thermoelectric applications [4].

 doi:10.20944/preprints202601.1941.v1

While many Zintl pnictides have already been studied as potential thermoelectrics, the majority of the reports have been dedicated toward the characterization of antimonides [4]. By comparison, Zintl arsenides are less-studied, with only a few publications reporting transport or magnetic properties [7], although computational works have predicted increased thermoelectric performance for several arsenide systems [7–9], as well as the experimentally validated interesting physical properties like colossal magnetoresistance, anomalous Hall effect, and superconductivity [10–17].

Herein, we expand the field of Zintl arsenides by reporting, for the first time, the synthesis and the structural characterization of a novel Zintl phase, $Eu_9Zn_{4.5}As_9$. We present a detailed analysis of the crystal structure, the first of its kind, as well as its computed electronic band structure. As the chemical formula indicates, this compound belongs to the class of so-called "9–4–9" phases, $A_9M_{4+x}Pn_9$ (A = Ca, Sr, Eu, Yb; M = Mg, Mn, Zn, Cd; Pn = As, Sb, Bi). This family series is compositionally diverse and comprises several different structural types. Importantly, several "9–4–9" phases are well known as highly efficient thermoelectric materials with potential for dupability and excellent transport properties (Table 1).

Table 1. All reported (to date) ternary compositions and their multinary derivatives within the 9–4–9 family of compounds.

Compound	Space Group	References
$Ca_9Mn_{4+x}Bi_9$	*Pbam*	[18]
$Ca_9Zn_{4+x}Sb_9$; $(Ca,Yb)_9(Zn,Cu)_{4+x}Sb_9$	*Pbam*	[19–23]
$Ca_9(Zn,In)_{4+x}Sb_9$	*Amm2*[a] $P\bar{6}$[a] $P\bar{6}2m$[a]	[24]
$Ca_9(Cd,M)_{4+x}Sb_9$ (M = Zn, Al)	$P\bar{6}2m$[a]	[25]
$Ca_9Zn_{4+x}Bi_9$	*Pbam*	[18,26]
$Ca_9Cd_{4+x}Bi_9$	*Pbam*	[19,26]
$Ca_9(Mn,Al)_{4+x}Sb_9$	*Pbam*	[27]
$Sr_9Cd_{4+x}Sb_9$	*Pbam*	[26]
$Sr_9Cd_{4+x}Bi_9$	*Pbam*	[19,26]
$Eu_9Cd_{4+x}Bi_9$, $Eu_9(Cd,M)_{4+x}Bi_9$ (M = Cu, Ag, Au)	*Pbam*	[26,28]
$Yb_9Mn_{4+x}Sb_9$, $Yb_9(Mn,M)_{4+x}Sb_9$ (M = Zn, Al)	*Pbam*	[27,29,30]
$Yb_9Mn_{4+x}Bi_9$	*Pbam*	[27]
$Yb_9Zn_{4+x}Sb_9$	*Pbam*	[20]
$Yb_9Zn_{4+x}Bi_9$	*Pbam*	[26,31]
$Yb_9Cd_{4+x}Bi_9$	*Pbam*	[26]
$Eu_9(Mn,Al)_{4+x}Sb_9$	*Cmca*[b]	[30]
$Ca_9Mn_{4+x}Sb_9$,	*Pnma*[c]	[32]
$Ca_9Zn_{4+x}As_9$	*Pnma*[c]	[32]
$Sr_9Mg_{4+x}Sb_9$	*Pnma*[c]	[33]
$Sr_9Mg_{4+x}Bi_9$	*Pnma*[c]	[33]
$Eu_9Zn_{4+x}As_9$	*Pnma*[c]	This work

[a] The *Amm2* modification can be thought of as a supercell of the *Pbam* modification (standardized unit cell parameters [$a \approx 12$ Å; $b \approx 22$ Å, $c \approx 4$ Å]), where the relationship between the two can be expressed as $a' \approx c$, $b' \approx 3b$, and $c' \approx a$. The $P\bar{6}$ modification is related through $a'' \approx a\sqrt{3}$, $c'' \approx c$. $P\bar{6}2m$ is the average basic hexagonal structure of *Amm2* and $P\bar{6}$ superstructures with the relationship given as: $a''' \approx a$, and $c''' \approx c$.

[b] The *Cmca* modification can be thought of as a supercell of the *Pbam* modification, where the relationship between the two can be expressed as $a'''' \approx 2c$, $b'''' \approx b$, and $c'''' \approx 2a$.

[c] The *Pnma* modification can be thought of as a supercell of the *Pbam* modification, where the relationship between the two can be expressed as $a''''' \approx a$, $b''''' \approx c$, and $c''''' \approx 2b$.

 doi:10.20944/preprints202601.1941.v1

2. Materials and Methods

2.1 Synthesis

The ternary arsenide $Eu_9Zn_{4.5}As_9$ was originally discovered during attempts to optimize the synthesis of the Zintl arsenide Eu_3ZnAs_3 [34], and later heteroanionic Zintl arsenide oxide, $Eu_{14}Zn_5As_{12}O$ [35]. The following procedure can be utilized to synthesize large needle-like crystals (Figure 1) of the title phase. Europium metal pieces (Edgetech Ind., 99%), zinc shot (Sigma-Aldrich, 99.9%), arsenic granules (ThermoFisher, 99.999%), and tin shot (Thermo Scientific, 99.8%) were combined in a 5:1:3:20 molar ratio and placed in an alumina crucible. Europium pieces were filed prior to use to remove oxidized coatings. All materials were handled inside an argon-filled glove box to prevent degradation (H_2O and $O_2 \leq 1$ ppm). The loaded alumina crucible was then sealed within an evacuated fused silica ampoule topped with the quartz wool, which acts as a filter. The reactants were then heated to 1000°C and held for 24 h before being slowly cooled to 650°C and centrifuged to remove metal flux excess. The ampoules were then cracked open inside the glovebox.

This approach leads to the formation of large (≥ 1 mm) needle-like crystals of $Eu_9Zn_{4.5}As_9$, which are black in color and very brittle. Crystals of this compound can also be obtained using other approaches, as discussed in Section 3.1. Crystals were found to be air- and moisture-stable for at least several days. Suitable crystals were selected from the reaction product for both single-crystal X-ray diffraction and magnetic studies.

CAUTION! Arsenic and arsenic-containing compounds should be handled in proper personal protective equipment. Reactions must be conducted in well-ventilated areas, as reaction temperatures above the sublimation point of arsenic (614 °C) can produce dangerous byproducts. Arsenic tends to hydrolyze and create arsane gas, which is highly toxic; crucibles should not be immediately cleaned with water. Slow oxidation under the fume hood is advised.

2.2 Structural characterization

Structural characterization of the $Eu_9Zn_{4.5}As_9$ phase was carried out using single-crystal X-ray diffraction (SCXRD) methods. Data were collected using a Bruker D8 Venture DUO diffractometer (Bruker, Billerica, MA, USA) equipped with a Photon III C14 detector and Ag Kα radiation microfocus tube (λ = 0.56086 Å). Small black needle-like crystals were selected from the reaction product and mounted on a MiTiGen loop attached to the goniometer. A constant cold (100 K) nitrogen flow was applied to the crystal during data collection to protect the material from potential degradation due to contact with air and moisture. After collection, the data were processed using the SAINT and SADABS programs (version 2.03) from the APEX4 software suite [36,37]. The crystal structure was solved using intrinsic phasing with SHELXT (version 2018/2) and further refined via full-matrix least-squares on F^2 with SHELXL (version 2018/3) [38,39]. Olex2 (version 1.5) was used as a GUI for structure determination [40]. Finally, atomic coordinates were standardized using the STRUCTURE TIDY software [41]. Selected crystallographic data, including data collection details, atomic coordinates, and bond distances, can be found in Tables 2–4.

Table 2. Selected data collection details and crystallographic data for $Eu_9Zn_{4.5}As_9$ (T = 100(2) K)

Chemical formula	$Eu_9Zn_{4.5}As_9$
fw/g mol^{-1}	2336.08
Space group	*Pnma*
a/(Å)	12.1953(7)
b/(Å)	4.3730(2)
c/(Å)	42.674(2)
V (Å^3)	2275.8(2)
Z	4
$\rho_{cal.}$/g cm^{-3}	6.818

 doi:10.20944/preprints202601.1941.v1

μ(Ag K$_\alpha$)/ cm^{-1}	221.19
Collected/independent reflections	33102/4501
R_1 (I>2$\sigma_{(I)}$)[a]	0.0191
wR_2 (I>2$\sigma_{(I)}$)[a]	0.0348
R_1 (all data)[a]	0.0217
wR_2 (all data)[a]	0.0356
$\Delta\rho_{max,min}$/e$^-$·Å^{-3}	1.95/−1.24
CCDC code	2523214

[a] $R_1 = \Sigma||F_o|-|F_c||/\Sigma|F_o|$. $wR_2 = \{\Sigma[w(F_o^2 - F_c^2)^2]/\Sigma w F_o^4\}^{1/2}$, $w = 1/[\sigma^2(F_o^2) + (13.4340P)]$, where $P = (F_o^2 + 2F_c^2)/3$.

Table 3. Fractional atomic coordinates and equivalent isotropic displacement parameters U_{eq} values for $Eu_9Zn_{4.5}As_9$.

Atoms	Site	x	y	z	U_{eq}[a] (Å^2)
Eu1[b]	8d	0.02077(3)	0.17365(8)	0.58230(2)	0.00749(7)
Eu2[b]	8d	0.36020(3)	0.20624(17)	0.00124(2)	0.012(17)
Eu3	4c	0.03523(2)	1/4	0.67579(2)	0.00733(5)
Eu4	4c	0.04118(2)	1/4	0.19032(2)	0.00876(5)
Eu5	4c	0.06394(2)	1/4	0.04691(2)	0.01449(6)
Eu6	4c	0.23374(2)	1/4	0.32735(2)	0.00802(5)
Eu7	4c	0.28181(2)	1/4	0.42064(2)	0.01059(5)
Eu8	4c	0.30237(2)	1/4	0.24745(2)	0.00891(5)
Eu9	4c	0.31121(2)	1/4	0.62266(2)	0.00575(5)
Zn1[b]	4c	0.0749(1)	1/4	0.38646(3)	0.0076(2)
Zn2	4c	0.09963(5)	1/4	0.86014(2)	0.0069(1)
Zn3[b]	4c	0.2755(1)	1/4	0.17782(3)	0.0069(2)
Zn4B[c]	4c	0.3015(1)	1/4	0.49314(3)	0.0132(2)
Zn4A[c]	4c	0.3646(1)	1/4	0.50040(3)	0.0132(2)
Zn5[b]	4c	0.3303(1)	1/4	0.07027(3)	0.0073(2)
Zn6	4c	0.44570(5)	1/4	0.74422(2)	0.0070(1)
As1A[c]	4c	0.04713(9)	1/4	0.45177(2)	0.0083(1)
As1B[c]	4c	0.08877(9)	1/4	0.46353(3)	0.0083(1)
As2	4c	0.05186(4)	1/4	0.27507(2)	0.00597(9)
As3	4c	0.12226(4)	1/4	0.79615(2)	0.00485(8)
As4	4c	0.25374(4)	1/4	0.55010(2)	0.00599(9)
As5	4c	0.28296(4)	1/4	0.70105(2)	0.00565(9)
As6	4c	0.31521(4)	1/4	0.87441(2)	0.00710(9)
As7	4c	0.37576(4)	1/4	0.12899(2)	0.00743(9)
As8	4c	0.49340(4)	1/4	0.37946(2)	0.00564(9)
As9	4c	0.61590(5)	1/4	0.52913(2)	0.0097(1)

[a] U_{eq} is defined as one-third of the trace of the orthogonalized U_{ij} tensor.

[b] Site Occupancy Factors (SOFs) constrained at 0.5: Zn1; Zn3; Zn5; Eu1 and Eu2 are offset from the mirror plane with original coordinates of (4c: 0.0208, 1/4, 0.5823 for Eu1; 4c: 0.3604, 1/4, 0.0013 for Eu2);

[c] Refined Site Occupancy Factors (SOFs): 1 = 0.4858(15)Zn4A + 0.5142Zn4B; 1 = 0.5216(12)As1A + 0.4784As1B.

Table 4. Selected interatomic distances in $Eu_9Zn_{4.5}As_9$

Atom pair	Distance (Å)	Atom pair	Distance (Å)
Zn1–As1A	2.808(2)	Zn4B–As1B	2.886(2)
Zn1–As6 × 2	2.6154(7)	Zn4B–As4	2.500(1)
Zn1–As7	2.517(1)	Zn4B–As9 × 2	2.5879(8)

 doi:10.20944/preprints202601.1941.v1

Zn2–As3	2.7444(7)	Zn5–As1A	2.807(2)
Zn2–As6	2.6988(8)	Zn5–As4 × 2	2.5634(7)
Zn2–As8 × 2	2.5977(4)	Zn5–As7	2.566(1)
Zn3–As5 × 2	2.5043(6)	Zn6–As2 × 2	2.5525(4)
Zn3–As7	2.416(1)	Zn6–As3	2.7574(8)
Zn4A–As4	2.515(1)	Zn6–As5	2.7079(8)
Zn4A–As9 × 2	2.5348(7)		

2.3 Electronic Structure Calculations

Electronic structure calculations were performed by employing the density functional theory (DFT) using the Vienna Ab Initio Simulation Package (VASP) (version 6.4.3) [42]. The Perdew–Burke–Ernzerhof (PBE) exchange–correlation energy with the generalized gradient approximation (GGA) was employed for calculations [43]. Both core and valence electrons were treated with the projector-augmented wave method, with the Eu_2 pseudopotential used to consider Eu in the +2 configuration [44]. Structure optimization was performed prior to calculating the density of states and band structures. A Gamma-centered mesh of 8 × 3 × 1 points in the Brillouin zone generated by VASPKIT and an energy cutoff of 430 eV with a convergence tolerance of 1×10^{-6} eV/atom was used for self-consistent field calculations [45].

As disorder cannot be accounted for in VASP, a disorder-free model had to be designed in order to perform the calculations. With a goal of preserving charge-balanced composition, the split As1A/As1B and Zn4A/Zn4B positions were consolidated into single, fully occupied sites (As1 and Zn4) by averaging the refined atomic coordinates. Similarly, with both the Eu1 and Eu2 8*d* sites modeled as 50% occupied, we returned to the 4*c* fully occupied sites located on the mirror plane with coordinates listed in the footnote to Table 3. This model was again refined with SHELXL to ensure the accuracy of the newly applied coordinates. Finally, the half-occupied Zn sites (Zn1, Zn3, and Zn5) had to be addressed. As this disorder could not be easily resolved by treating these sites as fully occupied, the symmetry of the model was reduced from *Pnma* to $Pmn2_1$ in order to split each Zn position (Wyckoff 4*c*) into two distinct positions (Wyckoff 2*a*) with the help of the ISODISTORT tool [46,47]. From there, half of the newly split Zn1, Zn3, and Zn5 sites were removed, and the remaining atoms were set to fully occupied. This method produced both a structurally comparable and charge-balanced model suitable for calculations.

2.4 Magnetic Properties Measurements

Magnetic susceptibility was measured using a Quantum Design PPMS DynaCool system equipped with a 9 T Vibrating Sample Magnetometer (VSM). A suitable single crystal of $Eu_9Zn_{4.5}As_9$ was selected and checked with the SCXRD method to confirm the identity of the sample prior to property studies. The crystal was then cleaned of flux residue and washed with hexane. It was then mounted on the sample holder and fixed using GE varnish glue. Temperature-dependent measurements were obtained with a magnetic field of 1 kOe applied along the *b*-axis over a temperature range from 1.8 K to 300 K under both zero-field-cooling (ZFC) and field-cooling (FC) conditions. Magnetic isotherms were measured at 2 K, 6.5 K, 11 K, 15.5 K, and 20 K with applied magnetic fields varying from 0 Oe to 90 kOe.

3. Results and Discussion

3.1. Synthesis

As was mentioned in Section 2.1, the initial goal of the experiment that led us to the discovery of $Eu_9Zn_{4.5}As_9$ was to optimize the synthetic conditions for the growth of single crystals of the heteroanionic $Eu_{14}Zn_5As_{12}O$ [35] Zintl arsenide oxide. The attempt instead led to the formation of a new, previously unreported compound, later identified as the title phase. $Eu_9Zn_{4.5}As_9$ was also

 doi:10.20944/preprints202601.1941.v1

identified from our efforts to obtain single-phase Eu_3ZnAs_3 [34]. In both cases, $Eu_9Zn_{4.5}As_9$ was observed as a minor phase. To obtain the title compound in higher yields, several other synthetic methods were employed. Here, we caution that direct reactions of the elements in sealed Nb tubes are not suitable for high-temperature work with As[48], although many previously reported "9–4–9" compounds (Table 1) can be synthesized by this method.

Since there have been successful reports using lead or antimony molten fluxes to grow large single crystals [32,33], our subsequent efforts involved the former. Pb-flux, indeed, also yielded $Eu_9Zn_{4.5}As_9$ crystals over various component ratios and at temperatures ranging from 900° C to 1100° C. However, in most cases, the reactions afforded multiphase products with tiny crystals of the title phase, suitable for SCXRD studies but not for property studies. By comparison, crystals obtained by the tin-flux method at similar conditions reached lengths of up to 3 mm, making them suitable for property characterization.

Another synthetic challenge worth mentioning here is the heavily populated Eu–Zn–As compositional space with already six reported ternary phases, $EuZn_2As_2$ [49], $Eu_2Zn_2As_3$ [50], $Eu_{11}Zn_6As_{12}$ [51], Eu_3ZnAs_3 [34], $Eu_{21}Zn_4As_{18}$ [52,53], $Eu_{14}Zn_{1+x}As_{11}$ [54], alongside multiple binaries (Figure 1). The discovered compound falls between $Eu_{11}Zn_6As_{12}$ [51] and Eu_3ZnAs_3 phases [34], which explains the presence of the latter as common impurity phases.

Interestingly, most of the reported ternary compounds in the Eu–Zn–As phase diagram possess unusual thermoelectric, electrical, and magnetic properties, as was exemplified for $EuZn_2As_2$ [55–59], $Eu_2Zn_2As_3$ [50], $Eu_{11}Zn_6As_{12}$ [51], $Eu_{21}Zn_4As_{18}$ [60], and $Eu_{14}Zn_{1+x}As_{11}$ [61]. Arguably, further investigation of this compound will be warranted, which may yield the discovery of new and interesting physical properties.

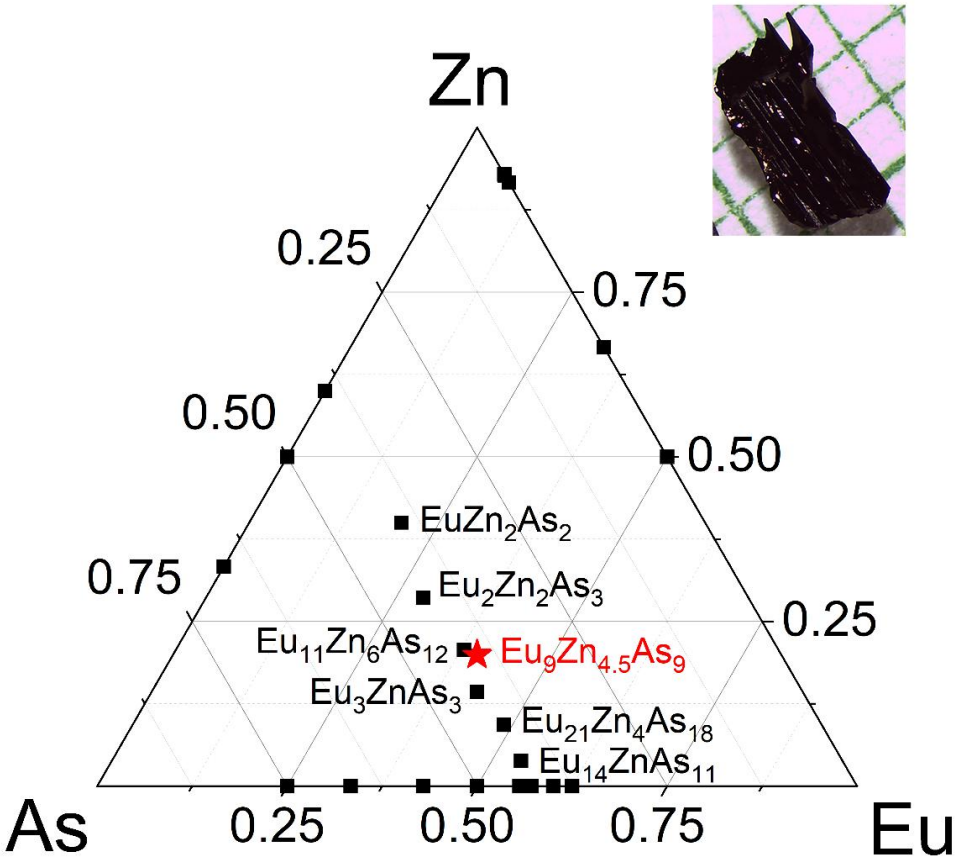

Figure 1. Ternary Eu–Zn–As compositional diagram. The newly discovered $Eu_9Zn_{4.5}As_9$ phase is marked as a red star. The insert shows the optical image of the synthesized needle-like crystal.

 doi:10.20944/preprints202601.1941.v1

3.2. Crystal Structure and Bonding

Formally, the structure of $Eu_9Zn_{4.5}As_9$ belongs to the $Ca_9Mn_{4+x}Sb_9$ structure type (space group *Pnma*, Table 1) [32], although it has its own nuances, specifically, it is more disordered. In light of this, the structural description here will be brief, focusing on differences from the archetype.

Being only the second Zintl arsenide (apart from $Ca_9Zn_{4+x}As_9$) belonging to the 9–4–9 family (Table 1), the title $Eu_9Zn_{4.5}As_9$ phase exemplifies a rare example of so-called 9–4–9 "supercell" [32,33] with a doubled unit cell volume, compared to the majority of the reported $A_9M_{4+x}Pn_9$ compositions (A = Ca, Sr, Ba, Eu, Yb; M = Mn, Zn, Cd; Pn = Sb, Bi, Table 1). Interestingly, recently discovered Mg-bearing $Sr_9Mg_{4+x}Pn_9$ (Pn = Sb, Bi) phases [33] are also isostructural to the "supercell" structure presented herein.

As can be expected, the unit cell volume of the $Eu_9Zn_{4.5}As_9$ phase (~2276 Å^3) is slightly larger than that of the only isostructural arsenide analog, $Ca_9Zn_{4+x}As_9$ (~2255 Å^3) [32]. This difference is due to the larger atomic radius of Eu (1.98 Å) compared to that of Ca (1.76 Å) [62]. As a general rule, the majority of $A_9M_{4+x}Pn_9$ compounds favor smaller cations, such as Ca or Yb, and, in fewer instances, larger Sr and Eu have been found to form phases with these structures (Table 1). On this note, $Eu_9Zn_{4.5}As_9$ exemplifies the first Eu-bearing 9–4–9 Zintl arsenide.

The schematic view of the orthorhombic crystal structure of $Eu_9Zn_{4.5}As_9$ is shown in Figure 2a. The imaginary, disorderless structure can be described with the Wyckoff sequence c^{24}, with 9 crystallographically independent Eu sites, 6 Zn sites, and 9 As sites all occupying special 4*c* positions. However, if all atomic positions are considered with full site occupancy factors (SOF), the resulting composition of $(Eu^{2+})_9(Zn^{2+})_6(As^{-3})_9$ would significantly depart from being charge-balanced. On the other hand, the common trait of the structural chemistry of 9–4–9 compounds is the presence of partially occupied M sites (M = Mg, Mn, Zn, Cd), as inferred from the non-stoichiometric $A_9M_{4+x}Pn_9$ (though close to charge-balanced) compositions, quantified by the "x" value.

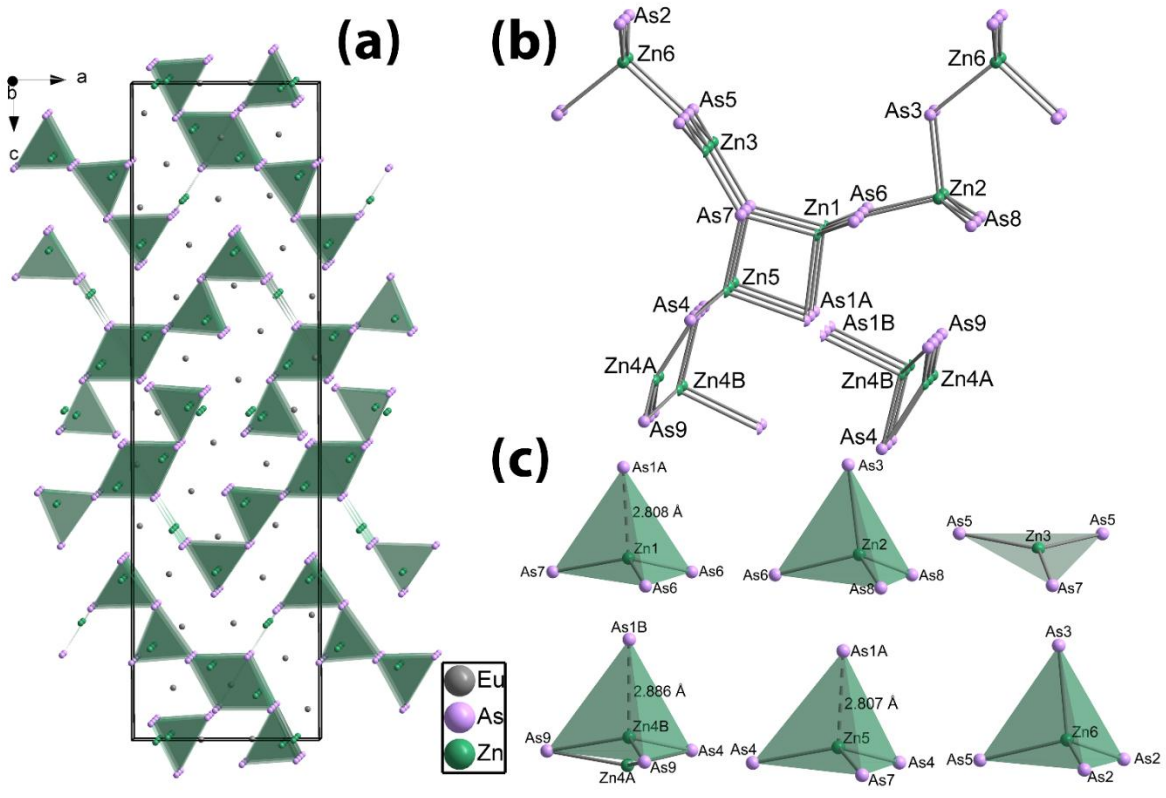

Figure 2. (a) Schematic representation of the unit cell of $Eu_9Zn_{4.5}As_9$, viewed along the *b*-axis. The unit cell is outlined. The structure is drawn in polyhedral representation with marked [$ZnAs_3$] trigonal-planar and [$ZnAs_4$] tetrahedral units. (b) A close-up view of the anionic substructure depicting all six Zn-centered polyhedra that contribute to the $[Zn_9As_{18}]^{36-}$ layers. Partially occupied/split sites are shown as defect-site sectors aligned with

 doi:10.20944/preprints202601.1941.v1

refined/constrained occupancies. (c) Zn-centered coordination polyhedra for all six crystallographically unique Zn sites. Eu atoms are shown in gray, Zn atoms are green, and As atoms are lavender.

The $Eu_9Zn_{4.5}As_9$ structure is not an exception, and it contains three Zn sites (Zn1, Zn3, and Zn5) with fractional SOFs of 0.485(3), 0.486(3), and 0.499(3), respectively, should they be refined unconstrained. Since all these values are very close to 0.5 (within 5σ), we have fixed their occupancies to 50%. Assuming divalent Eu (which is confirmed by our magnetic property studies, *vide infra*), this model yields the charge-balanced $(Eu^{2+})_9(Zn^{2+})_{4.5}(As^{-3})_9$ composition.

We do not, however, exclude the possibility that occupancies of these three Zn sites may vary from sample to sample, leading to $Eu_9Zn_{4+x}As_9$ compositions in which the x value slightly deviates from 0.5, akin to previously reported $Sr_9Mn_{4.45(1)}Bi_9$ and $Ca_9Mn_{4.46(1)}As_9$ [32]. Despite the predicted (semi)metallic behavior of the title compound, as discussed in Section 3.3, these small differences may slightly alter charge-carrier concentration and transport properties, similarly to the previously reported studies of thermoelectric properties of several other 9–4–9s [22,25,30,33,63,64]. In this context, the isovalent and aliovalent doping of these interstitial atoms can be viewed as an efficient mechanism to alter electrical transport properties and, therefore, potentially increase thermoelectric performance.

In addition, two Eu sites, Eu1 and Eu2, were modeled as split 8*d* sites, each with SOF of 0.5, due to the offset from the *ac* mirror plane. The 50% occupancy of Zn1 and Zn5 sites correlates with the split on Eu1 site, as shown in Figure 3b, in analogy to the previous reports on $Sr_9Mn_{4.45(1)}Bi_9$ and $Ca_9Mn_{4.46(1)}As_9$ [32]. The split on the Eu2 site, although less pronounced (as can be judged from the deviation of the y coordinate from ¼, Table 3), is not observed in these previously reported isostructural compounds for Sr2 and Ca2, making the title phase more disordered. This split, however, correlates with the concomitant split of Zn4 and As1 sites as illustrated in Figure 3c. Both sites were refined initially anisotropically and showed significantly elongated thermal ellipsoids, so after the modeled "split", their occupancies were found to be very close to 0.5 (Table 3), comparable with the previous reports on $Sr_9Mn_{4.45(1)}Bi_9$ and $Ca_9Mn_{4.46(1)}As_9$. The correlation between positional disorder at the As1 and Eu1/Eu2 sites is also apparent, assuming that the As1 atom is octahedrally coordinated by Eu atoms, as shown in Figure 3c.

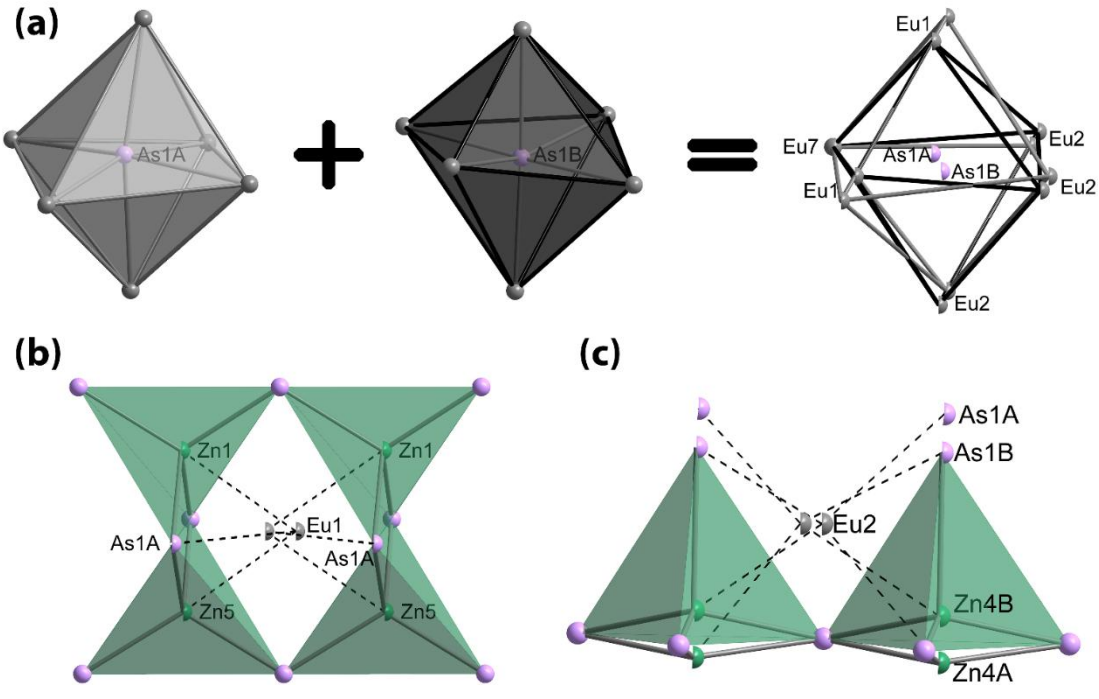

Figure 3. (a) Close-up view of the disorder around the As1 split site. The rightmost image shows the superposition of both As1A- and As1B-centered distorted octahedra composed of Eu7 and split Eu1/Eu7 sites.

 doi:10.20944/preprints202601.1941.v1

(b) Close-up view of the correlated disorder around the split Eu1 site. (c) Close-up view of the correlated disorder around split Eu2 sites. Feasible Eu–Zn and Eu–As contacts are marked as dashed lines. The color code is the same as in Figure 2.

The elongation of the thermal parameter on As1 and consequent split to As1A and As1B positions is necessary to complete the tetrahedral coordination of partially occupied Zn4B, Zn1, and Zn5 (Figure 2c), avoiding unrealistically long interatomic Zn–As distances (Table 4). Such disorder is quite common for Zintl pnictides, and the nearly identical local structure arrangement was recently reported for the $Eu_{14}Zn_5As_{12}O$ phase [35].

Due to the lack of homoatomic As–As bonds, the anionic substructure of $Eu_9Zn_{4.5}As_9$ is exclusively composed of Zn-centered polyhedra (Figure 2b). As shown in previous works, the unique crystal chemistry of Zn-bearing Zintl phases mainly originates from the versatility of Zn atoms to coordinate pnictogens in trigonal-planar and tetrahedral fashion [10,34,35,54,65–68]. In most cases, a partially occupied Zn site is associated with trigonal planar coordination, whereas fully occupied atoms tend to be tetrahedrally coordinated. While this is not always the case, as was recently shown for the Sr_3ZnAs_3 phase [34], the occupancy of metal often dictates the degree of protrusion from the As_3 plane. In Figure 2c, the local coordination environments of all Zn sites are presented. Only for the fully occupied Zn2 and Zn6 atoms, the longest Zn–As contact does not exceed 2.76 Å, which is somewhat longer than the sum of covalent radii of Zn and As (~2.41 Å) [62], yet still indicates a sizable interaction. These two atoms also protrude the most from the As_3 plane (~0.76 Å for Zn2 and 0.68 Å for Zn6), whereas the protrusion does not exceed ~0.56 Å for the partially occupied Zn atoms. The corresponding bond lengths fall in a wide range (Table 4), with all values being comparable to the previous reports [49–54].

The corner- and edge-sharing arrangement of these $[ZnAs_4]$ and $[ZnAs_3]$ units (Figure 2c) composes the anionic substructure of $Eu_9Zn_{4.5}As_9$, which can be described as a series of $[Zn_9As_{18}]^{36-}$ layers stacked along the *c*-direction (Figure 2a,b) and was discussed in a detailed manner in the previous works [32,33]. Apparently, the 2D dimensionality of this assembly can be partially broken due to multiple partially occupied Zn and As sites, as exemplified in Figure 4b, which represents the disordered-free model used for the electronic structure calculations, *vide infra*. This needs to be considered when drawing structure-property relationships in the context of electronic and thermal transport. For instance, extensive disorder may reduce the lattice thermal conductivity, whereas doping with cations that prefer tetrahedral coordination, such as Al^{3+}, Mn^{2+}, or In^{3+}, may prevent the dimensionality reduction and positively affect transport properties. These results will be presented in future studies.

At last, we would like to briefly discuss the complex arrangement of the lattice made of magnetic Eu^{2+} cations (Figure 4a). It is mainly composed of three main building units, typical for Zintl pnictides: (i) trigonal $[Eu_6]$ prisms, both empty and filled with As anions, (ii) distorted $[Eu_6]$ octahedra, that host disordered As1 atoms, and (iii) empty $[As_4]$ tetrahedra. There are several relatively close Eu–Eu contacts (shorter than 4.0 Å), which can be an indication of complex magnetic interactions and, potentially, anisotropy of the magnetic response.

 doi:10.20944/preprints202601.1941.v1

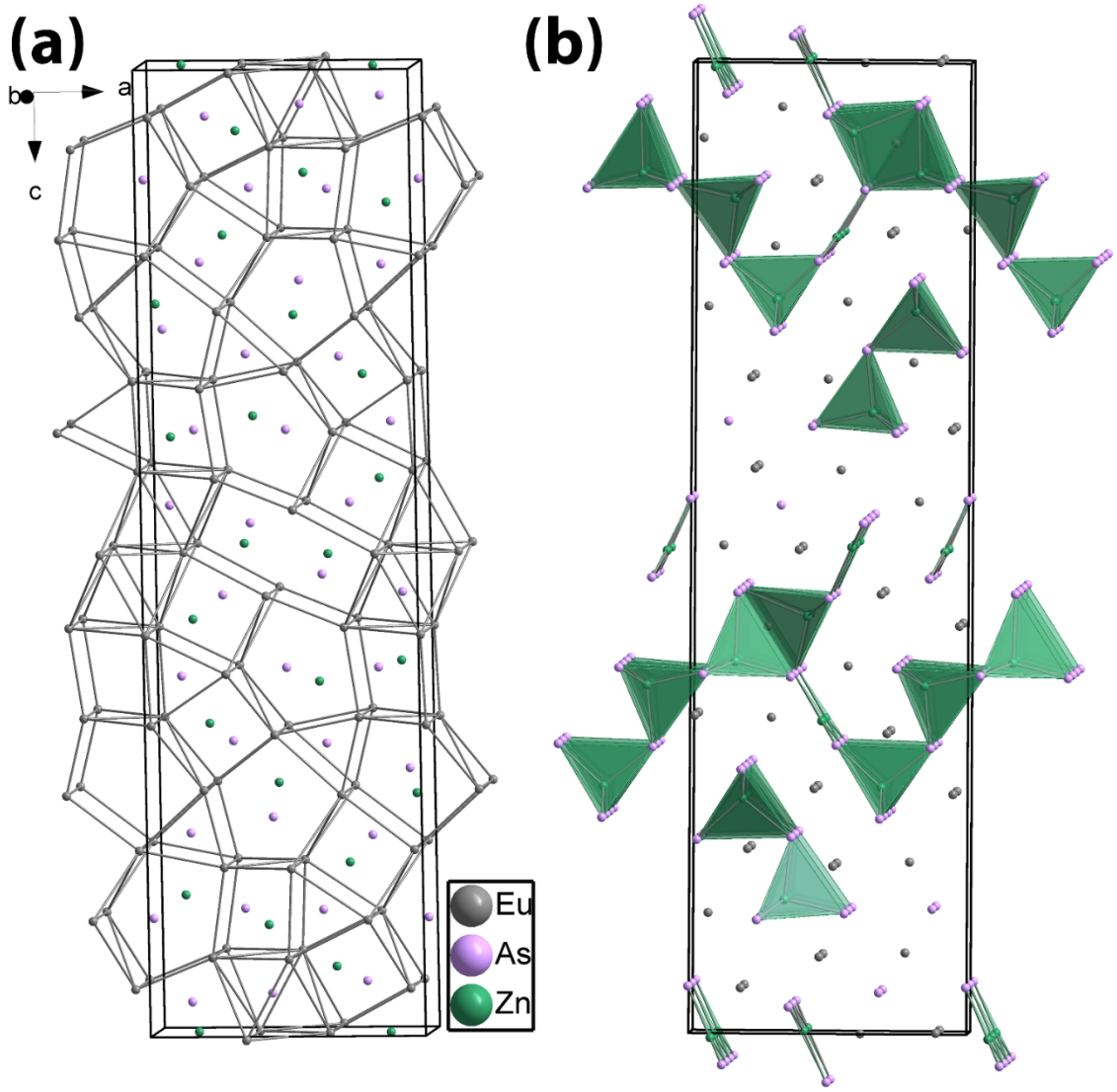

Figure 4. (a) Idealized orthorhombic structure of $Eu_9Zn_{4.5}As_9$ highlighting the complex scaffold of magnetic Eu^{2+} ions. The cutoff for the Eu–Eu contacts is ~4.43 Å. (b) ISODISTORT-derived disorder-free model of $Eu_9Zn_{4.5}As_9$ used for the electronic structure calculations (space group *Pmn*2_1) drawn in polyhedral representation, emphasizing Zn-based tetrahedral and trigonal planar units. The color code is the same as in Figure 2. The unit cells are outlined.

3.3 Electronic Structure

As discussed in the experimental section, a supercell model had to be constructed in order to address partially occupied sites when performing calculations on $Eu_9Zn_{4.5}As_9$. This model is schematically represented in Figure 4b. Figure 5 shows the calculated density of states (DOS) and band structure for the title phase in the energy range of –5 to 2 eV. The Fermi level is set at 0 eV and indicated by the dashed line. A small pseudogap is observed in the DOS plot at the Fermi level.

Following the earlier discussion, the $Eu_9Zn_{4.5}As_9$ formula is charge-balanced, and one should expect the bulk material to be a semiconductor, possibly with a narrow bandgap. From general considerations, viz., the electronegativity differences between the respective elements, many other Eu, Zn, and As-based materials should fall within the realm of semiconducting behavior. Yet, these expectations are only partially corroborated by the electronic structure calculations for $Eu_9Zn_{4.5}As_9$, where the gapless DOS plot indicates semimetallic behavior. A possible explanation for it is the partial covalency of the Eu–As interactions, which is not captured by the fully ionic $(Eu^{2+})_9(Zn^{2+})_{4.5}(As^{3-})_9$ description, Evidence in support of this conjecture are the partial DOS curves, which show that Eu–p and Eu–d orbitals make up the majority of states below the Fermi level, with

 doi:10.20944/preprints202601.1941.v1

a lesser contribution from Zn–p and As–p states. The total and partial DOS plots exhibit features similar to those of other reported ternary Zintl pnictides [53].

Also of note is the fact that in the band structure of $Eu_9Zn_{4.5}As_9$, along the *Y*–Γ path (Figure 5c), the bands come extremely close to one another without crossing to form Dirac-like linearized points. This band feature has been found in other ternary topological insulating Zintl phases, such as EuAuSb [69], $EuCd_2As_2$ [70], and $CaIn_2As_2$ [11], which could indicate $Eu_9Zn_{4.5}As_9$ as a possible nontrivial topological material. Computational studies exploring the role of spin-orbit coupling (SOC) and symmetry analyses, as well as more in-depth physical property measurements, could shed further light on the title phase's electronic structure, however these studies are beyond the scope of this work and will not be addressed here.

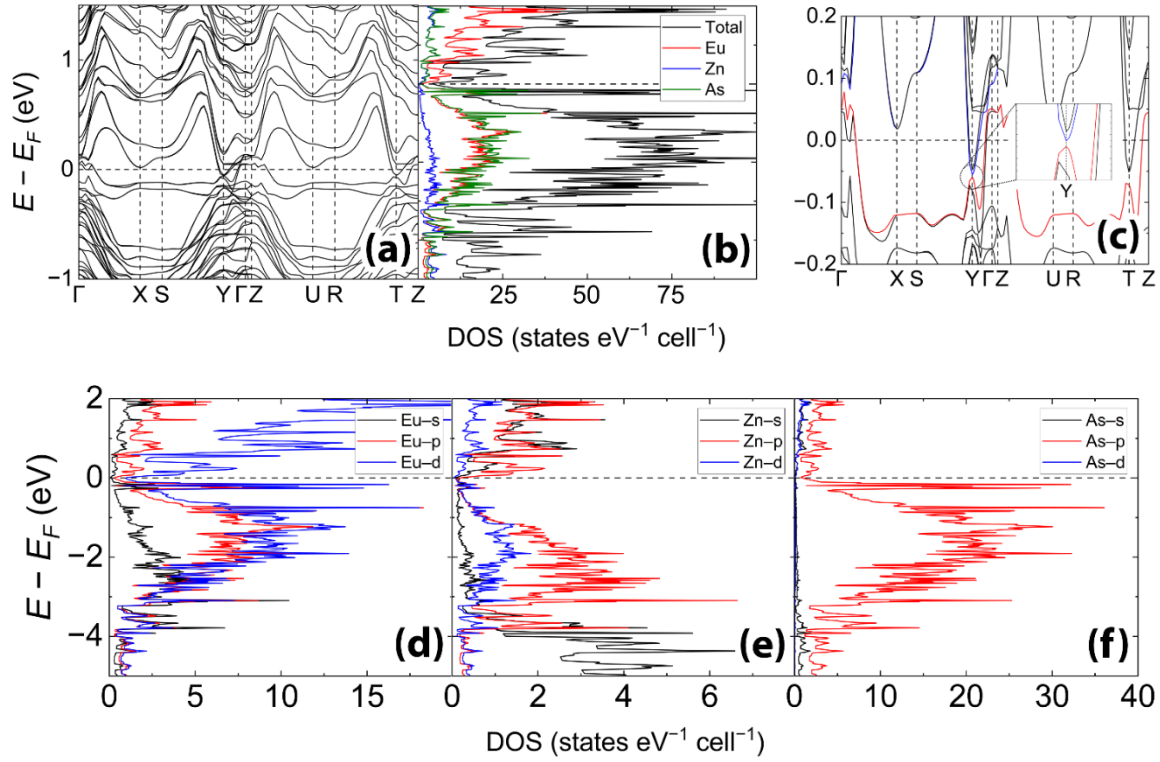

Figure 5. Calculated (a) band structure, (b) total density of states (DOS), and partial (PDOS) density of states for (d) Eu, (e) Zn, (f) As. An enlarged view of the band structure near the Fermi level is shown in (c) with the Dirac-like point at the *Y* k-point. The Fermi level is set at 0 eV as an energy reference.

3.4. Magnetic Properties

Temperature-dependent magnetic susceptibility of single-crystal $Eu_9Zn_{4.5}As_9$ was measured under a magnetic field of 1 kOe applied along the b axis using both zero-field-cooled (ZFC) and field-cooled (FC) protocols (Figure 6a). At high temperatures, the magnetic susceptibility of $Eu_9Zn_{4.5}As_9$ is well described by Curie–Weiss behavior (1)

$$\chi(T) = C/(T - \theta_{CW}) \quad (1)$$

where *C* represents the Curie constant (emu·mol^{-1}·K^{-1}), given by $C = N_A\mu_{eff}^2/3k_B$ (N_A is Avogadro's number, μ_{eff} is the effective magnetic moment, k_B is the Boltzmann constant), and θ_{CW} denotes the Curie-Weiss temperature [71]. A fit to the susceptibility data over the temperature range 50–300 K yields an effective magnetic moment μ_{eff} = 7.9 μ_B and Weiss constant θ_{CW} = −2.15 K. The extracted effective moment is in excellent agreement with the theoretical free-ion value μ_{th} = 7.94 μ_B expected for divalent Eu^{2+} ions with electronic configuration [Xe] $4f^7$, total angular momentum *J*=7/2 , and Landé factor *g*=2 [72]. The magnetization measurement further shows a saturation moment consistent with the theoretical value $\mu_{sat} = g\,J\,\mu_B$ = 7.0 μ_B per Eu^{2+} ion (Figure 6b).

 doi:10.20944/preprints202601.1941.v1

Upon cooling, the magnetic susceptibility of $Eu_9Zn_{4.5}As_9$ exhibits a pronounced anomaly at the Néel temperature T_N = 7.3 K (Figure 6a, inset), marking the onset of antiferromagnetic order. Below T_N, a weak feature appears in the field-cooled susceptibility data near 4.9 K, accompanied by a small ZFC–FC bifurcation. Previously reported Eu-bearing 9–4–9 phases, $Eu_9Cd_{4.2}Bi_9$ [26] and $Eu_9Cd_{4.45}Sb_9$ [32], exhibit similar antiferromagnetic transitions at T_N = 11 K and 10 K, respectively. Multiple other Eu-bearing Zintl arsenides also exhibit the antiferromagnetic transition, which is a common trait for Zintl chemistry of Eu [30,73–83]. In contrast, the Yb-containing representatives of this family display simple paramagnetic behavior along the low-temperature range [26,27].

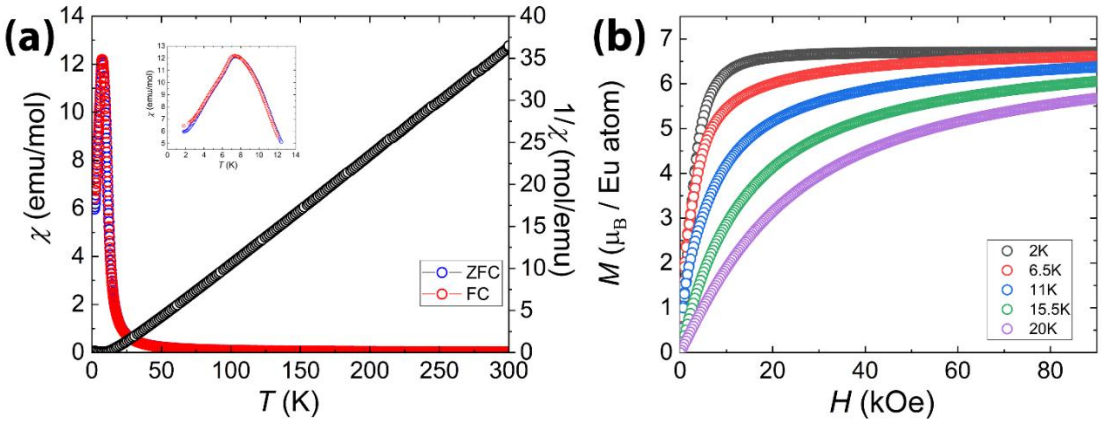

Figure 6. Magnetic properties of a single crystal of $Eu_9Zn_{4.5}As_9$. (a) Magnetic susceptibility (χ and χ^{-1}), measured over the temperature range from 1.8 K to 300 K under zero-field-cooling (ZFC) and field-cooling (FC) conditions. (b) Magnetization isotherms measured at 2 K, 6.5K, 11 K, 15.5 K, and 20 K.

4. Conclusions

In this work, we have introduced another member of the heavily populated Eu–Zn–As system—a new Eu-bearing Zintl arsenide, $Eu_9Zn_{4.5}As_9$. This compound has a complex, heavily disordered crystal structure, although the disorder is necessary to achieve a charge-balanced composition. Electronic structure calculations predict that this compound will likely behave like a (semi)metal, which, together with the presence of a complex framework of magnetic Eu^{2+} species, could lead to interesting physical properties, such as colossal magnetoresistance, complex magnetic interactions, or other quantum phenomena typical of other Zintl phases with such features. In addition, this compound can be thoroughly doped with iso-and aliovalent metal cations, such as Cd^{2+}, Mn^{2+}, Mg^{2+}, Al^{3+}, Ga^{3+}, and In^{3+}, which may open the possibility for excellent thermoelectric performance, which will be studied in the following works.

Author Contributions: Methodology, conceptualization, supervision S.B. (S. Baranets); investigation, formal analysis, visualization S.W., O.P., and S.B. (S. Baranets); validation, S.W., O.P.; data curation, S.W., O.P., and B.T.; writing—original draft preparation, S.W. and O.P.; writing—review and editing, project administration, funding acquisition S.B. (S. Baranets), S.B. (S. Bobev), and X.B.; S.B. Authors have read and agreed to the published version of the manuscript.

Funding: S. Baranets acknowledges financial support from the U.S. National Science Foundation under Award No. DMR-2440354 and from the Louisiana State Board of Regents under Award LEQSF (2024-27)-RD-A-06. S. Bobev acknowledges financial support from the United States Department of Energy, Office of Science, Basic Energy Sciences, under Award #DE-SC0008885. X. Bai acknowledges financial support from the U.S. Department of Energy, Office of Science, Basic Energy Sciences, under Award Number DE-SC002542. X-ray crystallographic data were collected by the diffractometer funded by the NSF MRI award CHE-2215262.

Data Availability Statement: The corresponding crystallographic information files (CIF) have been deposited with the Cambridge Crystallographic Database Centre (CCDC) and can be obtained free of charge via https://www.ccdc.cam.ac.uk/structures/ or by emailing data_request@ccdc.cam.ac.uk with the following depository number: 2523214. Other raw data is available upon request.

Conflicts of Interest: The authors declare no conflicts of interest.

 doi:10.20944/preprints202601.1941.v1

References

1. Nesper, R. The Zintl-Klemm concept–a historical survey. *Z. Anorg. Allg. Chem.* **2014**, *640*, 2639-2648.
2. Kauzlarich, S.M. Zintl phases: From curiosities to impactful materials. *Chem. Mater.* **2023**, *35*, 7355-7362.
3. Ovchinnikov, A.; Bobev, S. Zintl phases with group 15 elements and the transition metals: A brief overview of pnictides with diverse and complex structures. *J. Solid State Chem.* **2019**, *270*, 346-359.
4. Liu, K.-F.; Xia, S.-Q. Recent progresses on thermoelectric Zintl phases: Structures, materials and optimization. *J. Solid State Chem.* **2019**, *270*, 252-264.
5. Kauzlarich, S.M.; Zevalkink, A.; Toberer, E.; Snyder, G.J. Zintl phases: recent developments in thermoelectrics and future outlook. In *Thermoelectric Materials and Devices*; 2016.
6. Kauzlarich, S.M.; Devlin, K.P.; Perez, C.J. Zintl phases for thermoelectric applications. In *Thermoelectric Energy Conversion*; Elsevier: 2021; pp. 157-182.
7. Islam, M.M.; Kauzlarich, S.M. The Potential of Arsenic-based Zintl Phases as Thermoelectric Materials: Structure & Thermoelectric Properties. *Z. Anorg. Allg. Chem.* **2023**, *649*, e202300149.
8. Luo, D.B.; Wang, Y.X.; Yan, Y.L.; Yang, G.; Yang, J.M. The high thermopower of the Zintl compound $Sr_5Sn_2As_6$ over a wide temperature range: first-principles calculations. *J. Mater. Chem.* **2014**, *2*, 15159-15167.
9. Yan, Y.L.; Wang, Y.X.; Zhang, G.B. Electronic structure and thermoelectric performance of Zintl compound $Ca_5Ga_2As_6$. *J. Mater. Chem.* **2012**, *22*, 20284-20290.
10. Devlin, K.P.; Kazem, N.; Zaikina, J.V.; Cooley, J.A.; Badger, J.R.; Fettinger, J.C.; Taufour, V.; Kauzlarich, S.M. $Eu_{11}Zn_4Sn_2As_{12}$: a ferromagnetic Zintl semiconductor with a layered structure featuring extended Zn_4As_6 Sheets and ethane-like Sn_2As_6 units. *Chem. Mater.* **2018**, *30*, 7067-7076.
11. Ogunbunmi, M.O.; Baranets, S.; Childs, A.B.; Bobev, S. The Zintl phases AIn_2As_2 (A= Ca, Sr, Ba): new topological insulators and thermoelectric material candidates. *Dalton Trans.* **2021**, *50*, 9173-9184.
12. Li, H.; Gao, W.; Chen, Z.; Chu, W.; Nie, Y.; Ma, S.; Han, Y.; Wu, M.; Li, T.; Niu, Q. Magnetic properties of the layered magnetic topological insulator $EuSn_2As_2$. *Phys. Rev. B* **2021**, *104*, 054435.
13. Xu, Y.; Song, Z.; Wang, Z.; Weng, H.; Dai, X. Higher-order topology of the axion insulator $EuIn_2As_2$. *Phys. Rev. Lett.* **2019**, *122*, 256402.
14. Zhou, Z.; Wang, Z.; Chen, X.; Lu, J.-Y.; Zhang, J.; Luo, X.; Cao, G.-H.; Dong, S.; Wang, Z.-C. Unusual magnetic and transport properties in the Zintl phase $Eu_{11}Zn_6As_{12}$. *Phys. Rev. Mater.* **2024**, *8*, 114421.
15. Cao, W.; Yang, H.; Li, Y.; Pei, C.; Wang, Q.; Zhao, Y.; Li, C.; Zhang, M.; Zhu, S.; Wu, J. Pressure-induced superconductivity in the Zintl topological insulator $SrIn_2As_2$. *Phys. Rev. B* **2023**, *108*, 224510.
16. Rotter, M.; Pangerl, M.; Tegel, M.; Johrendt, D. Superconductivity and crystal structures of $(Ba_{1-x}K_x)Fe_2As_2$ (x= 0–1). *Angew. Chem. Int. Ed.* **2008**, *47*, 7949-7952.
17. Balguri, S.; Mahendru, M.B.; Delgado, E.O.G.; Fruhling, K.; Yao, X.; Graf, D.E.; Rodriguez-Rivera, J.A.; Aczel, A.A.; Hicken, T.J.; Luetkens, H. Two types of colossal magnetoresistance with distinct mechanisms in $Eu_5In_2As_6$. *Phys. Rev. B* **2025**, *111*, 115114.
18. Brechtel, E.; Cordier, G.; Schafer, H. Darstellung und kristallstruktur von $Ca_9Mn_4Bi_9$ und $Ca_9Zn_4Bi_9$/preparation and crystal structure of $Ca_9Mn_4Bi_9$ and $Ca_9Zn_4Bi_9$. *Z. Naturforsch. B* **1979**, *34*, 1229-1233.
19. Brechtel, E.; Cordier, G.; Schäfer, H. Neue Verbindungen mit der $Ca_9Mi_4Bi_9$-Struktur: Zur Kenntnis von $Ca_9Cd_4Bi_9$, $Sr_9Cd_4Bi_9$ und $Ca_9Zn_4Sb_9$/New Compounds with the $Ca_9Mn_4Bi_9$ Structure: $Ca_9Cd_4Bi_9$, $Sr_9Cd_4Bi_9$, and $Ca_9Zn_4Sb_9$. *Z. Naturforsch. B* **1981**, *36*, 1099-1104.
20. Bobev, S.; Thompson, J.D.; Sarrao, J.L.; Olmstead, M.M.; Hope, H.; Kauzlarich, S.M. Probing the Limits of the Zintl Concept: structure and bonding in rare-earth and alkaline-earth zinc-antimonides $Yb_9Zn_{4+x}Sb_9$ and $Ca_9Zn_{4.5}Sb_9$. *Inorg. Chem.* **2004**, *43*, 5044-5052.
21. Chen, C.; Xue, W.; Li, X.; Lan, Y.; Zhang, Z.; Wang, X.; Zhang, F.; Yao, H.; Li, S.; Sui, J. Enhanced Thermoelectric Performance of Zintl Phase $Ca_9Zn_{4+x}Sb_9$ by Beneficial Disorder on the Selective Cationic Site. *ACS Appl. Mater. Interfaces* **2019**.
22. Ohno, S.; Aydemir, U.; Amsler, M.; Pöhls, J.H.; Chanakian, S.; Zevalkink, A.; White, M.A.; Bux, S.K.; Wolverton, C.; Snyder, G.J. Achieving zT> 1 in inexpensive zintl phase $Ca_9Zn_{4+x}Sb_9$ by phase boundary mapping. *Adv. Funct. Mater.* **2017**, *27*, 1606361.

 doi:10.20944/preprints202601.1941.v1

23. Seo, N.; Lee, J.; Lee, Y.; Choi, M.-H.; Pi, J.H.; Lee, K.H.; Ok, K.M.; You, T.-S. Synergistic effect of cation substitution and p-type anion doping to improve thermoelectric properties in Zintl phases. *Energy Mater.* **2025**, *5*, 500123.
24. Smiadak, D.M.; Baranets, S.; Rylko, M.; Marshall, M.; Calderón-Cueva, M.; Bobev, S.; Zevalkink, A. Single crystal growth and characterization of new Zintl phase $Ca_9Zn_{3.1}In_{0.9}Sb_9$. *J. Solid State Chem.* **2021**, *296*, 121947.
25. Lee, J.; Kim, M.; Pi, J.H.; Choi, M.-H.; Ok, K.M.; Lee, K.H.; You, T.-S. Insights into the Crystal Structure and Thermoelectric Properties of the Zintl Phase $Ca_9Cd_{3+x-y}M_{x+y}Sb_9$ (M= Cu, Zn) System. *Chem. Mater.* **2024**, *37*, 368-377.
26. Xia, S.-q.; Bobev, S. Interplay between Size and Electronic Effects in Determining the Homogeneity Range of the $A_9Zn_{4+x}Pn_9$ and $A_9Cd_{4+x}Pn_9$ Phases ($0 \leq x \leq 0.5$), A= Ca, Sr, Yb, Eu; Pn= Sb, Bi. *J. Am. Chem. Soc.* **2007**, *129*, 10011-10018.
27. Xia, S.-Q.; Bobev, S. New manganese-bearing antimonides and bismuthides with complex structures. Synthesis, structural characterization, and electronic properties of $Yb_9Mn_{4+x}Pn_9$ (Pn= Sb or Bi). *Chem. Mater.* **2010**, *22*, 840-850.
28. Kazem, N.; Hurtado, A.; Klobes, B.; Hermann, R.l.P.; Kauzlarich, S.M. $Eu_9Cd_{4-x}CM_{2+x-y}\square_ySb_9$: $Ca_9Mn_4Bi_9$-Type Structure Stuffed with Coinage Metals (Cu, Ag, and Au) and the Challenges with Classical Valence Theory in Describing These Possible Zintl Phases. *Inorg. Chem.* **2015**, *54*, 850-859.
29. Bux, S.K.; Zevalkink, A.; Janka, O.; Uhl, D.; Kauzlarich, S.; Snyder, J.G.; Fleurial, J.-P. Glass-like lattice thermal conductivity and high thermoelectric efficiency in $Yb_9Mn_{4.2}Sb_9$. *J. Mater. Chem.* **2014**, *2*, 215-220.
30. Liu, X.-C.; Liu, K.-F.; Wang, Q.-Q.; Wang, Y.-M.; Pan, M.-Y.; Xia, S.-Q. Exploring New Zintl Phases in the 9-4-9 Family via Al Substitution. Synthesis, Structure, and Physical Properties of $Ae_9Mn_{4-x}Al_xSb_9$ (Ae= Ca, Yb, Eu). *Inorg. Chem.* **2020**, *59*, 3709-3717.
31. Kim, S.-J.; Salvador, J.; Bilc, D.; Mahanti, S.; Kanatzidis, M.G. $Yb_9Zn_4Bi_9$: Extension of the Zintl concept to the mixed-valent spectator cations. *J. Am. Chem. Soc.* **2001**, *123*, 12704-12705.
32. Liu, X.-C.; Wu, Z.; Xia, S.-Q.; Tao, X.-T.; Bobev, S. Structural variability versus structural flexibility. A case study of $Eu_9Cd_{4+x}Sb_9$ and $Ca_9Mn_{4+x}Sb_9$ ($x \approx 1/2$). *Inorg. Chem.* **2015**, *54*, 947-955.
33. Zhang, J.; Liu, Q.; Liu, K.-F.; Tan, W.-J.; Liu, X.-C.; Xia, S.-Q. $Sr_9Mg_{4.45(1)}Bi_9$ and $Sr_9Mg_{4.42(1)}Sb_9$: Mg-containing Zintl phases with low thermal conductivity. *Inorg. Chem.* **2021**, *60*, 4026-4033.
34. Baranets, S.; Balvanz, A.; Darone, G.M.; Bobev, S. On the effects of aliovalent substitutions in thermoelectric Zintl pnictides. varied polyanionic dimensionality and complex structural transformations—the case of Sr_3ZnP_3 vs $Sr_3Al_xZn_{1-x}P_3$. *Chem. Mater.* **2022**, *34*, 4172-4185.
35. Ishtiyak, M.; Watts, S.R.; Thipe, B.; Womack, F.; Adams, P.; Bai, X.; Young, D.P.; Bobev, S.; Baranets, S. Advancing Heteroanionicity in Zintl Phases: Crystal Structures, Thermoelectric and Magnetic Properties of Two Quaternary Semiconducting Arsenide Oxides, $Eu_8Zn_2As_6O$ and $Eu_{14}Zn_5As_{12}O$. *Inorg. Chem.* **2024**, *63*, 20226-20239.
36. *SAINT*, BrukerAXS Inc.: 2014.
37. *SADABS*, BrukerAXS Inc.: 2014.
38. Sheldrick, G.M. SHELXT–Integrated space-group and crystal-structure determination. *Acta Crystallogr. Sect. A* **2015**, *71*, 3-8.
39. Sheldrick, G.M. Crystal structure refinement with SHELXL. *Acta Crystallogr. Sect. C* **2015**, *71*, 3-8.
40. Dolomanov, O.V.; Bourhis, L.J.; Gildea, R.J.; Howard, J.A.; Puschmann, H. OLEX2: a complete structure solution, refinement and analysis program. *J. Appl. Crystallogr.* **2009**, *42*, 339-341.
41. Gelato, L.; Parthé, E. STRUCTURE TIDY–a computer program to standardize crystal structure data. *J. Appl. Crystallogr.* **1987**, *20*, 139-143.
42. Kresse, G.; Furthmüller, J. Efficient iterative schemes for ab initio total-energy calculations using a plane-wave basis set. *Phys. Rev. B* **1996**, *54*, 11169.
43. Perdew, J.P.; Ruzsinszky, A.; Csonka, G.I.; Vydrov, O.A.; Scuseria, G.E.; Constantin, L.A.; Zhou, X.; Burke, K. Generalized gradient approximation for solids and their surfaces. *J. Phys. Chem. Lett.* **2007**.
44. Blöchl, P.E. Projector augmented-wave method. *Phys. Rev. B* **1994**, *50*, 17953.
45. Wang, V.; Xu, N.; Liu, J.-C.; Tang, G.; Geng, W.-T. VASPKIT: A user-friendly interface facilitating high-throughput computing and analysis using VASP code. *Comput. Phys. Commun.* **2021**, *267*, 108033.

46. Campbell, B.J.; Stokes, H.T.; Tanner, D.E.; Hatch, D.M. ISODISPLACE: a web-based tool for exploring structural distortions. *Appl. Crystallogr.* **2006**, *39*, 607-614.
47. H. T. Stokes, D.M.H., and B. J. Campbell *ISOTROPY Software Suite*, iso.byu.edu.
48. Baranets, S.; He, H.; Bobev, S. Niobium-bearing arsenides and germanides from elemental mixtures not involving niobium: a new twist to an old problem in solid-state synthesis. *Cryst. Struct. Commun.* **2018**, *74*, 623-627.
49. Klüfers, P.; Neumann, H.; Mewis, A.; SCHUSTER, H. AB_2X_2-Verbindungen im $CaAl_2Si$+-Typ. VIII. **1980**.
50. Stoyko, S.S.; Khatun, M.; Mar, A. Ternary arsenides $A_2Zn_2As_3$ (A= Sr, Eu) and their stuffed derivatives $A_2Ag_2ZnAs_3$. *Inorg. Chem.* **2012**, *51*, 2621-2628.
51. Saparov, B.; Bobev, S. Undecaeuropium hexazinc dodecaarsenide. *Struct. Rep.* **2010**, *66*, i24-i24.
52. Suen, N.-T.; Wang, Y.; Bobev, S. Synthesis, crystal structures, and physical properties of the new Zintl phases $A_{21}Zn_4Pn_{18}$ (A= Ca, Eu; Pn= As, Sb)—Versatile arrangements of $[ZnPn_4]$ tetrahedra. *J. Solid State Chem.* **2015**, *227*, 204-211.
53. Ishtiyak, M.; Watts, S.R.; Pokhvata, O.; Kandabadage, T.; Baranets, S. Complex Structural Disorder in Thermoelectric Zintl Phases $Eu_{21}M_4As_{18}$ (M= Mn, Zn). *Z. Anorg. Allg. Chem.* **2025**, *651*, e202500070.
54. Baranets, S.; Darone, G.M.; Bobev, S. Synthesis and structure of $Sr_{14}Zn_{1+x}As_{11}$ and $Eu_{14}Zn_{1+x}As_{11}$ ($x \leq 0.5$). New members of the family of pnictides isotypic with $Ca_{14}AlSb_{11}$, exhibiting a new type of structural disorder. *J. Solid State Chem.* **2019**, *280*, 120990.
55. Kong, D.; Karbasizadeh, S.; Narasimha, G.; Regmi, P.; Tao, C.; Mu, S.; Vasudevan, R.; Harrison, I.; Jin, R.; Gai, Z. Large bandgap observed on the surfaces of $EuZn_2As_2$ single crystals. *Commun. Phys.* **2025**, *8*, 287.
56. Wang, Z.-C.; Been, E.; Gaudet, J.; Alqasseri, G.M.A.; Fruhling, K.; Yao, X.; Stuhr, U.; Zhu, Q.; Ren, Z.; Cui, Y. Anisotropy of the magnetic and transport properties of $EuZn_2As_2$. *Phys. Rev. B* **2022**, *105*, 165122.
57. Blawat, J.; Marshall, M.; Singleton, J.; Feng, E.; Cao, H.; Xie, W.; Jin, R. Unusual electrical and magnetic properties in layered $EuZn_2As_2$. *Adv. Quantum Technol.* **2022**, *5*, 2200012.
58. Bukowski, Z.; Rybicki, D.; Babij, M.; Przewoźnik, J.; Gondek, Ł.; Żukrowski, J.; Kapusta, C. Canted antiferromagnetic order in $EuZn_2As_2$ single crystals. *Sci. Rep.* **2022**, *12*, 14718.
59. Regmi, P.; Blawat, J.; Jin, R. Large unconventional Hall effect observed in $EuZn_2As_2$. *Phys. Rev. B* **2025**, *111*, 014422.
60. Islam, M.M.; Wróblewska, M.; Shen, Z.; Toberer, E.S.; Taufour, V.; Kauzlarich, S.M. Magnetism and Thermoelectric Properties of the Zintl Semiconductor: $Eu_{21}Zn_4As_{18}$. *Chem. Mater.* **2024**.
61. Islam, M.M.; Zheng, J.; Pike, A.; Star, K.E.; Bux, S.K.; Hautier, G.; Kauzlarich, S.M. Diffuson-Driven Lattice Thermal Conductivity in Zintl Arsenides: Disrupting Mass-Thermal Conductivity Relation for High Thermoelectric Performance. *J. Am. Chem. Soc.* **2025**, *147*, 42883-42893.
62. Cordero, B.; Gómez, V.; Platero-Prats, A.E.; Revés, M.; Echeverría, J.; Cremades, E.; Barragán, F.; Alvarez, S. Covalent radii revisited. *Dalton Trans.* **2008**, 2832-2838.
63. Xue, W.; Chen, C.; Nan, P.; Long, Y.; Ge, B.; Zhang, Q.; Wang, Y. Decoupling electrical conductivity and Seebeck coefficient via isoelectronic alloying in the 9-4-9-type $Ca_{9-y}Eu_yZn_{4.7}Sb_9$ ($0 \leq y \leq 5.0$) Zintl phase. *J. Mater. Chem.* **2026**.
64. Kazem, N.; Zaikina, J.V.; Ohno, S.; Snyder, G.J.; Kauzlarich, S.M. Coinage-metal-stuffed $Eu_9Cd_4Sb_9$: Metallic compounds with anomalous low thermal conductivities. *Chem. Mater.* **2015**, *27*, 7508-7519.
65. Wang, J.; Yox, P.; Voyles, J.; Kovnir, K. Synthesis, crystal structure, and properties of three La–Zn–P compounds with different dimensionalities of the Zn–P framework. *Cryst. Growth Des.* **2018**, *18*, 4076-4083.
66. Wilson, D.K.; Saparov, B.; Bobev, S. Synthesis, crystal structures and properties of the Zintl phases Sr_2ZnP_2, Sr_2ZnAs_2, A_2ZnSb_2 and A_2ZnBi_2 (A= Sr and Eu). *Z. Anorg. Allg. Chem.* **2011**, *637*, 2018-2025.
67. Gvozdetskyi, V.; Lee, S.J.; Owens-Baird, B.; Dolyniuk, J.-A.; Cox, T.; Wang, R.; Lin, Z.; Ho, K.-M.; Zaikina, J.V. Ternary Zinc Antimonides Unlocked Using Hydride Synthesis. *Inorg. Chem.* **2021**, *60*, 10686-10697.
68. Devlin, K.P.; Zhang, J.; Fettinger, J.C.; Choi, E.S.; Hauble, A.K.; Taufour, V.; Hermann, R.P.; Kauzlarich, S.M. Deconvoluting the Magnetic Structure of the Commensurately Modulated Quinary Zintl Phase $Eu_{11-x}Sr_xZn_4Sn_2As_{12}$. *Inorg. Chem.* **2021**, *60*, 5711-5723.

 doi:10.20944/preprints202601.1941.v1

69. Ram, D.; Singh, J.; Banerjee, S.; Sundaresan, A.; Samal, D.; Kanchana, V.; Hossain, Z. Magnetotransport and electronic structure of EuAuSb: A candidate antiferromagnetic Dirac semimetal. *Phys. Rev. B* **2024**, *109*, 155152.
70. Li, B.-X.; Song, Z.; Fang, Z.; Wang, Z.; Weng, H. Manipulation of topological phase transitions and the mechanism of magnetic interactions in Eu-based Zintl-phase materials. *Phys. Rev. B* **2025**, *111*, 205127.
71. Mugiraneza, S.; Hallas, A.M. Tutorial: a beginner's guide to interpreting magnetic susceptibility data with the Curie-Weiss law. *Commun. Phys.* **2022**, *5*, 95.
72. Kittel, C.; McEuen, P. *Introduction to solid state physics*; John Wiley & Sons: 2018.
73. Wu, D.; Na, S.; Li, Y.; Zhou, X.; Wu, W.; Song, Y.; Zheng, P.; Li, Z.; Luo, J. Single-crystal growth, structure and thermal transport properties of the metallic antiferromagnet Zintl-phase β-$EuIn_2As_2$. *Phys. Chem. Chem. Phys.* **2024**, *26*, 8695-8703.
74. Radzieowski, M.; Stegemann, F.; Klenner, S.; Zhang, Y.; Fokwa, B.P.; Janka, O. On the divalent character of the Eu atoms in the ternary zintl phases $Eu_5In_2Pn_6$ and Eu_3MAs_3 (Pn= As–Bi; M= Al, Ga). *Mater. Chem. Front.* **2020**, *4*, 1231-1248.
75. Weippert, V.; Haffner, A.; Stamatopoulos, A.; Johrendt, D. Supertetrahedral layers based on GaAs or InAs. *J. Am. Chem. Soc.* **2019**, *141*, 11245-11252.
76. Goforth, A.M.; Klavins, P.; Fettinger, J.C.; Kauzlarich, S.M. Magnetic properties and negative colossal magnetoresistance of the rare earth zintl phase $EuIn_2As_2$. *Inorg. Chem.* **2008**, *47*, 11048-11056.
77. Gebre, M.S.; Jiang, Z.; Riedel, Z.W.; Pappas, E.A.; Zhou, H.; Schleife, A.; Shoemaker, D.P. Unique structure type and antiferromagnetic ordering in semiconducting Eu_2InSnP_3. *Chem. Mater.* **2025**, *37*, 6118-6126.
78. Day, R.; Yamakawa, K.; Cairns, L.P.; Singleton, J.; Cao, W.; Wu, C.; Allen, M.; Moore, J.; Analytis, J.G. Colossal magnetoresistance and anisotropic spin dynamics in the antiferromagnetic semiconductor $Eu_5Sn_2As_6$. *Phys. Rev. B* **2025**, *111*, 054406.
79. Fender, S.; Thomas, S.; Ronning, F.; Bauer, E.; Thompson, J.; Rosa, P. Narrow-gap semiconducting behavior in antiferromagnetic $Eu_{11}InSb_9$. *Phys. Rev. Mater.* **2021**, *5*, 074603.
80. Wu, Y.; Li, T.; Chen, X.; Liu, Z.; Li, Y.; Shang, Z.; Zheng, X.; Tian, H.; Wang, Z.; Bi, Y. Surface Half-Metallicity and Electronic Structure Evolution in A-Type Antiferromagnet $EuIn_2P_2$. *Nano Lett.* **2025**.
81. Souza, J.C.; Thomas, S.; Bauer, E.; Thompson, J.; Ronning, F.; Pagliuso, P.; Rosa, P. Microscopic probe of magnetic polarons in antiferromagnetic $Eu_5In_2Sb_6$. *Phys. Rev. B* **2022**, *105*, 035135.
82. Ma, X.; Lu, J.; Whalen, J.B.; Latturner, S.E. Flux growth and magnetoresistance behavior of rare earth Zintl phase EuMgSn. *Inorg. Chem.* **2013**, *52*, 3342-3348.
83. Cook, M.S.; Peterson, E.A.; Kengle, C.S.; Kennedy, E.; Sheeran, J.; Girod, C.; Freitas, G.; Greer, S.M.; Abbamonte, P.; Pagliuso, P. Magnetic polaron formation in $EuZn_2P_2$. *Phys. Rev. Mater.* **2025**, *9*, 104403.